Uncertainty-Aware Trajectory Planning: Using Uncertainty Quantification and Propagation in Traversability Prediction of Planetary Rovers

Reiya Takemura[1] and Genya Ishigami[2]

I. Introduction

In an extreme environment such as Mars or a volcanic area, mobile robots have been used in scientific missions, or as precursors for a future manned mission. The robot called a planetary exploration rover is managed by a space-qualified, radiation-hardened, and low-clock onboard computer, and autonomously travels over challenging terrain. The rover often encounters mobility hazards such as vehicle rollover on a sloped terrain, collision with obstacles, or the wheels getting stuck in loose soil. These issues are addressed by rover traversability prediction in motion planning [1]. The prediction involves several indices, such as the wheel slip and posture angles on rough and loose terrains. Traversability indices are predicted based on the terrain feature information or interaction between the terrain surface and robot motion. Using the indices, the rover can carefully plan feasible motion within their traversability performance. Therefore, the traversability prediction is particularly important for rover's traveling autonomously on rough and loose terrains and needs to be processed with less computational time due to the limitation of the processing performance.

Previous studies have proposed motion planners that avoid the risky locomotion of the rover on rough and loose terrains based on its traversability indices [2]. Although the usefulness of motion planners using traversability prediction is experimentally validated, it is difficult to precisely predict robot traversability indices under uncertainty assumptions. Particularly, on rough and loose terrains, the modeling of the traversability prediction is subject to heteroscedastic uncertainties, such as the measurement uncertainty of onboard vision sensors and the motion uncertainty of the rover. Figure 1 depicts the heteroscedastic uncertainty environment, wherein rover state can be expressed by particles based on the traversability prediction model with different variances. These uncertainties often occur and cause the rover states to be stochastically distributed, which leads to an increase in the probability of mobility hazards.

To remedy this, we develop an uncertainty-aware trajectory planner for a planetary rover, including uncertainty quantification and propagation in the traversability prediction model. The major contributions are as follows:

- Uncertainty in a slip prediction model for a steered vehicle in high-slip conditions is experimentally measured.
- The slip uncertainty along with pose prediction uncertainty is quantified as two metrics with the idea of uncertainty propagation.
- Uncertainty metrics extend the conventional trajectory planner, enabling the rover to assess the growth of heteroscedastic uncertainty over the time steps.

The authors are with the Graduate School of Integrated Design Engineering, Keio University, Japan (e-mail: rereon@keio.jp; ishigami@mech.keio.ac.jp).

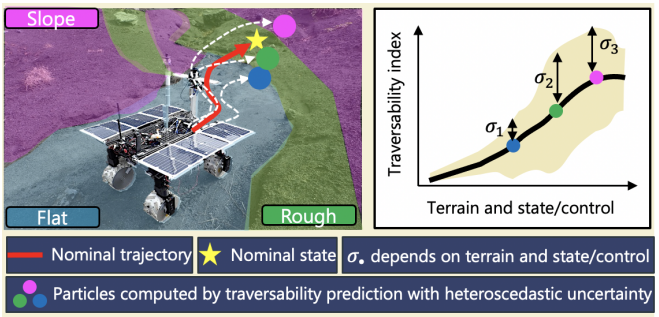

Fig. 1. State transition in heteroscedastic uncertainty environment consisting of various terrains such as slope, rough terrain, and flat areas. Left: When rover tracks a nominal trajectory, its state can be expressed by particles based on the traversability prediction under uncertainty assumption. Right: Traversability prediction model with heteroscedastic uncertainty described by different variances σ, which depend on terrain feature and rover state/control.

II. Related Research

There have been significant studies dealing with the uncertainty effect, where motion planning is conducted in the belief space [3]–[8]. In the space, the robot states are estimated by a belief, which is based on the probability distributions over the states. Particle rapidly-exploring random trees (RRT) can search for a feasible motion of a wheeled mobile robot, even under the assumption of uncertainty in rough terrain friction [3]. Motion uncertainty RRT is a robust motion planner against motion uncertainty measured by field experiments, which considers uncertainty propagation in multiple types of terrain [4]. Such particle-based approach iteratively predicts the growth of the robot state covariance using each particle in the presence of Gaussian uncertainty. Therefore, it can correctly describe the uncertainty expansion even in heteroscedastic uncertainty. However, the computational time of the particle-based planners is equivalent to that of the classical RRT algorithm multiplied by the number of particles; hence, the computational overhead is explicit. Conversely,

the confidence-ellipse-based approach is a computationally efficient method to approximate the effects of Gaussian uncertainty [5]. Rapidly-exploring random belief trees leverage the Kalman filter in a linear-quadratic-Gaussian (LQG) control to approximate the covariance of future states in the presence of the process and sensor noise [6]. The LQG motion planning (LQG-MP) evaluates the probabilistic distribution of a configuration throughout the generated path [7]. Lee et al. proposed a robust motion planner using LQG-MP to consider uncertainties in the position and heading due to vehicle slippage in deformable high-slip terrain [8]. These confidence-ellipse-based approach approximates the state covariance as a confidence ellipse; moreover, the growth of the ellipse is assessed to compute the probability of collision with obstacles. However, the confidence-ellipse-based approach cannot correctly express the uncertainty propagation because it hypothesizes that the uncertainty in the entire environment is homogeneous as explained in the previous study [4].

Uncertainty in traversability prediction has been addressed in connection with the motion planning problem [9]–[12]. Otsu et al. proposed the approximate clearance evaluation algorithm to estimate conservative bounds for the rover's pose on a patch of terrain [9]. The method assumes the uncertainty in terrain height underlying wheels; and, it exploits the lowest and highest heights for each wheel to calculate the worst-case vehicle configuration. Risk-aware motion planners based on the chance-constraint approach have also been developed by exploiting traversability prediction uncertainty [10], [11]. They assumes a heteroscedastic uncertainty in slip prediction model, which is expressed by Gaussian processes. In the planning process, the probability of vehicle immobilization on sandy slopes or rough terrains is assessed in the chance-constraint manner, which ensures that the probability is less than the threshold value. This approach is also known as Value at Risk (VaR) and one of the major risk assessment methods. While the uncertainty in the traversability prediction is well expressed, the propagation of heteroscedastic uncertainty over the time steps was not assessed appropriately, which may lead to inaccurate calculation for VaR. This is because the algorithms solve the problem as path planning, which is more discrete than trajectory planning. The details are explained in the following problem formulation. Recently, Cai et al. addressed risk-aware motion planning on multiple types of terrain with heteroscedastic uncertainty with Conditional VaR (CVaR) approach [12]. They exploit non-linear optimization planners such as Model Predictive Path Integral (MPPI), which can generate feasible motion/control set for reaching a goal. The MPPI is integrated with the CVaR approach, leading to a more conservative solution by pessimistically accounting for uncertainty. While this previous work greatly improves navigation success rate, it requires computational resources such as powerful CPU and GPU due to the use of the MPPI's optimization in the CVaR calculation.

Table I summarizes the difference between the problems addressed by the existing works. No existing study combines all of the items in the table, and particularly, the heteroscedastic uncertainty in the traversability prediction model makes the motion planning difficult. To address all items in the table, we propose an uncertainty-aware trajectory planner.

TABLE I

SUMMARY OF EXISTING RESEARCH EFFORTS ON MOTION PLANNING UNDER UNCERTAINTY ASSUMPTION.

	Particle	Ellipse	Traversability prediction	
	[3], [4]	[5]–[8]	[9]–[11]	[12]
Low computational cost		✓	✓	
Homogeneous uncertainty	✓	✓	✓	✓
Homogeneous unc. propagation	✓	✓	✓	✓
Heteroscedastic uncertainty	✓		✓	✓
Heteroscedastic unc. propagation	✓			✓
Traversability			✓	✓

III. Problem Formulation

We assume that a four-wheeled rover is equipped with a differential suspension and steerable front wheels as shown in Fig. 2. The state variable of the rover is expressed as follows:

$$\boldsymbol{x} = [x\ y\ \psi\ \phi\ \theta\ s\ \beta]^{\mathrm{T}}, \tag{1}$$

where x and y are the coordinates of the robot's center of gravity. ψ denotes the yaw angle of the robot. ϕ and θ are the roll and pitch angles of the rover, respectively, which show the pose angle. s is the vehicle slip ratio in the longitudinal direction of the rover. β denotes the vehicle sideslip angle. ϕ, θ, s, and β are subject to the traversability prediction uncertainty. Further, the environment is a rough terrain uniformly covered with loose soil. In such an environment, the rover needs to plan safe trajectories using the traversability prediction, consisting of pose and slip prediction models.

A. System Dynamics

Let $\boldsymbol{X}$ and $\boldsymbol{U}$ be the state space and the control input space of the rover. The stochastic system dynamics is described in a discrete time manner as follows:

$$\boldsymbol{x}_{n+1} = f(\boldsymbol{x}_n, \boldsymbol{u}_n, \boldsymbol{w}_n),\ \boldsymbol{w}_n \sim \mathcal{N}(\boldsymbol{0}, \boldsymbol{W}_n) \tag{2}$$

where the state $\boldsymbol{x}_n \in \boldsymbol{X}$ and control $\boldsymbol{u}_n \in \boldsymbol{U}$ describe the time evolution of the system dynamics from time n to $n+1$. The function $f(\cdot)$ indicates the state-transition based on the vehicle model and traversability prediction. The variable $\boldsymbol{w}_n$ is the process noise and is given by a zero-mean Gaussian distribution with covariance $\boldsymbol{W}_n$. In this study, the covariance represents the uncertainty caused in the pose and slip prediction models and they depend on terrain feature and robotic state/control. Owing to the process noise, the state $\boldsymbol{x}_n$ cannot be specified; hence, the state is described by *belief*, which consists of the existing probabilities ${}^k b$ for several states ${}^k \boldsymbol{x} \in \boldsymbol{x}_n$.

B. Trajectory Planning with Uncertainty Constraint

The objective of trajectory planning is to determine the sequential states of the rover to safely reach a set goal region.

$$\mathscr{T}^* = \arg\ \min\{C(\mathscr{T}) | \mathscr{T} = \{\hat{\boldsymbol{x}}_0, \cdots, \hat{\boldsymbol{x}}_n, \cdots, \hat{\boldsymbol{x}}_N\}\}, \tag{3}$$

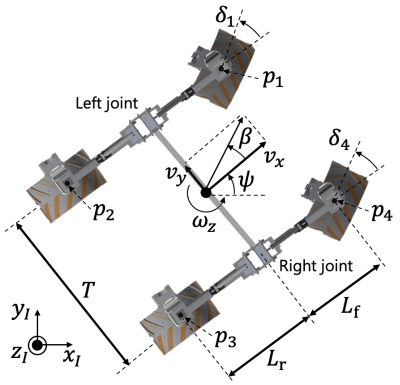

Fig. 2. Schematic view of the 2.5 dimensional vehicle model.

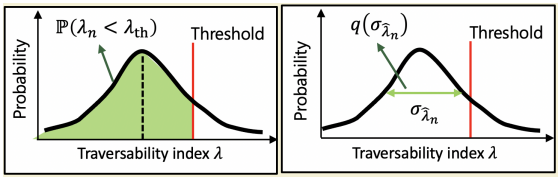

Fig. 3. Illustration for chance constraint (VaR) and uncertainty metrics. Left: VaR calculates probability for safe state using cumulative distribution and threshold. Right: Uncertainty metrics calculates q using the variance of probability distribution.

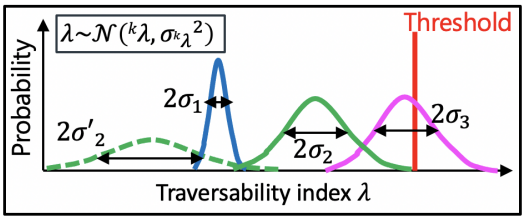

Fig. 4. Schematic interpretation of probability distributions for traversability prediction model under heteroscedastic uncertainty in Fig. 1. Each variance are determined by terrain features and rover state/control. Descending order: $\sigma'_2 > \sigma_2 = \sigma_3 > \sigma_1$.

$$C(\mathscr{T}) = \sum_{n=0}^{N} \left\{ W_l(\frac{l_n}{N_l})^2 + W_\phi(\frac{\hat{\phi}_n}{N_\phi})^2 + W_\theta(\frac{\hat{\theta}_n}{N_\theta})^2 + W_s(\frac{\hat{s}_n}{N_s})^2 + W_\beta(\frac{\hat{\beta}_n}{N_\beta})^2 \right\},$$

where $\hat{\boldsymbol{x}}_n$ is the nominal state calculated by $\hat{\boldsymbol{x}}_n = f(\hat{\boldsymbol{x}}_{n-1}, \hat{\boldsymbol{u}}_{n-1}, \boldsymbol{0})$, which is Eq. (2) without the process noise. $\mathscr{T}$ is the nominal trajectory, which is given by the sequence of the nominal states from the initial state $\hat{\boldsymbol{x}}_0 = \boldsymbol{x}_{\text{start}}$ to the goal state $\hat{\boldsymbol{x}}_N$ in $\boldsymbol{X}_{\text{goal}}$. $C(\mathscr{T})$ is a user-defined function that shows the cumulative cost for the the traversability indices throughout a nominal trajectory. l is the length of the trajectory. $N_\bullet$ and $W_\bullet$ are the normalization and weighting factors.

To assess the risk of mobility hazards under uncertainty assumption, the chance-constraint for vehicle rollover and wheel stuck on rough and loose terrain is expressed as follows:

$$\mathbb{P}(\bigwedge_n \lambda_n < \lambda_{\text{th}}) \geq p_{\text{safe}}, \ \forall n \in [0, N], \qquad \lambda \in [\phi, \theta, s, \beta] \quad (4)$$

where λ is traversability indices and λ_{th} is its threshold value. $\mathbb{P}(\cdot)$ represents the probability and is calculated as illustrated in the left in Left Fig. 3. p_{safe} describes the confidence level of traversability, which is used for VaR. Eq. (4) represents that the rover can probabilistically traverse within a certain confidence level against vehicle rollovers and wheel stucks. Previous works [10], [11] calculate the probability in Eq. (4) only from the nominal state. However, it is insufficient when the heteroscedastic uncertainty is assumed. To calculate the probability accurately, the probability that λ_n is less than λ_{th} needs to be considered for each state in *belief* as follows:

$$\mathbb{P}(\lambda_n < \lambda_{\text{th}}) = \int_0^{\lambda_{\text{th}}} p(\lambda_n) d\lambda_n = \iint_{{}^k\boldsymbol{x} \in \boldsymbol{x}_n}^{\lambda_{\text{th}}} p(\lambda_n, {}^k\boldsymbol{x}) d\lambda_n d^k\boldsymbol{x}$$

where $p(\cdot)$ is the probability distribution for traversability prediction model under heteroscedastic uncertainty. To simplify the equation, we can discretely expand the last term as follows:

$$\iint_{{}^k\boldsymbol{x} \in \boldsymbol{x}_n}^{\lambda_{\text{th}}} p(\lambda_n, {}^k\boldsymbol{x}) d\lambda_n d^k\boldsymbol{x} \simeq {}^0b \int_0^{\lambda_{\text{th}}} p(\lambda_n, {}^0\boldsymbol{x}) d\lambda_n + \ldots \quad (5)$$
$$+ {}^kb \int_0^{\lambda_{\text{th}}} p(\lambda_n, {}^k\boldsymbol{x}) d\lambda_n + \ldots + \hat{b} \int_0^{\lambda_{\text{th}}} p(\lambda_n, \hat{\boldsymbol{x}}) d\lambda_n + \ldots$$

where the existing probability ${}^kb$ meets $\sum_{{}^k\boldsymbol{x} \in \boldsymbol{x}_n} {}^kb = 1$. In our study, $p(\cdot)$ is given by the Gaussian distribution $\mathcal{N}({}^k\lambda, \sigma^2_{{}^k\lambda}(\mathscr{M}, {}^k\boldsymbol{x}, {}^k\boldsymbol{u}))$, where $\sigma^2_{{}^k\lambda}$ represents the variance and changes in response to terrain map $\mathscr{M}$, state ${}^k\boldsymbol{x}$, and control ${}^k\boldsymbol{u}$. Therefore, $p(\cdot)$ varies based on the heteroscedastic uncertainty as shown in Fig. 4. While each $p(\cdot)$ and ${}^kb$ are not negligible under heteroscedastic uncertainty, the calculation of all $p(\cdot)$ and ${}^kb$ is computationally expensive because the particle-based approach is required. In [10], [11], the term consisting of $p(\hat{\boldsymbol{x}})$ and $\hat{b}$ associated with the nominal state is only considered since a discrete path planning problem is assumed.

To prevent inaccurate calculation in Eq. (5) but to save computational cost, this study introduces the constraint of uncertainty metrics instead of the calculation of the probability in Eq. (4). The proposed constraint is described as follows:

$$q(\sigma_{\hat{\phi}_n}, \sigma_{\hat{\theta}_n}, \sigma_{\hat{s}_n}, \sigma_{\hat{\beta}_n}) \leq q_{\text{th}}, \ \forall n \in [0, N] \quad (6)$$

where q is the uncertainty metric, which shows the degree of uncertainty and is calculated based on the variance of traversability prediction model as shown in Right Fig. 3. q_{th} is the user-defined/risk-awareness parameter, which constrains the optimal trajectory planning instead of p_{safe}. Eq. (6) represents that the rover can solidly traverse within a smaller uncertainty effect for vehicle rollovers and wheel stucks. The background of the uncertainty metrics is that when the

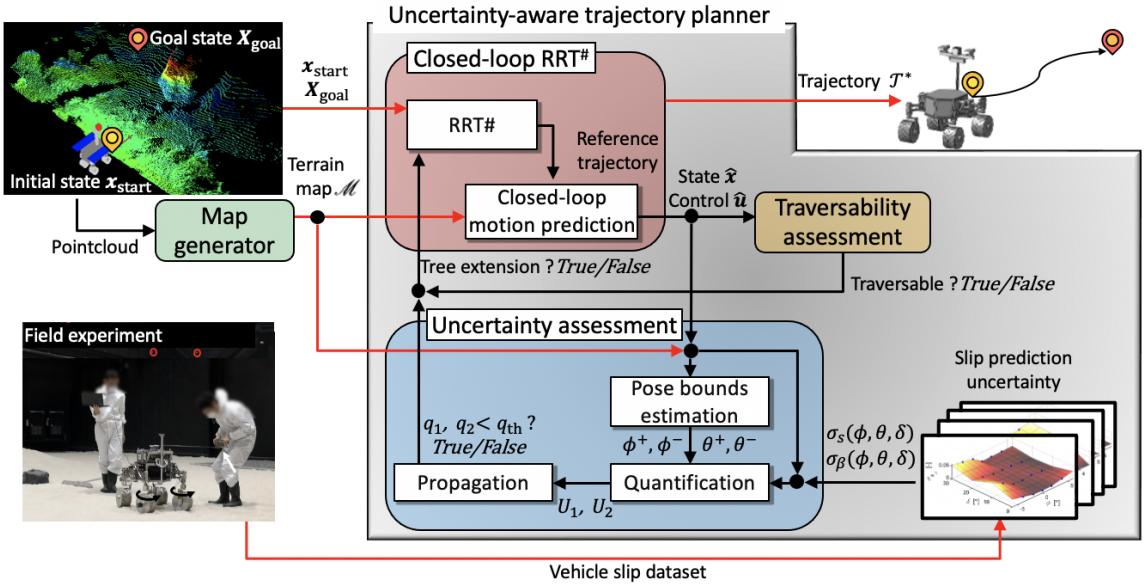

Fig. 5. Overview of the robot system involving the proposed uncertainty-aware trajectory planner.

variance $\sigma^2_{\hat{\lambda}_n}$ of the nominal state is large, $p(\cdot)$, and ${}^k b$ can be diverse due to heteroscedastic uncertainty propagation. This would possibly involves a tail risk for the rover mobility hazards. Overall, our proposed trajectory planning solves Eq. (3) under the constraint of Eqs. (2) and (6) to address the heteroscedastic uncertainty.

IV. Uncertainty-Aware Trajectory Planning

A. Overview

Figure 5 presents the robot system involving the uncertainty-aware planner. This study exploits the closed-loop RRT sharp (CL-RRT$^{\#}$), which does not require solving the two-point boundary value problem for a steered vehicle [13]. The proposed algorithm incorporates the traversability and uncertainty assessments into state tree extension in CL-RRT$^{\#}$. Firstly, the closed-loop motion prediction proposed in [14] (See Supplementary Materials) simulates the transition of Eq. 2 without the process noise. In the closed-loop simulation, the traversability indices are predicted; and, the traversability assessment examines tree extension for the nominal state by using each threshold value ϕ_{th}, θ_{th}, s_{th}, and β_{th} as in [14]. Subsequently, the uncertainty metrics are calculated to assess the state tree extension again, where uncertainty quantification and propagation expresses the degree of the uncertainty in pose and slip prediction models. The threshold value q_{th} limits the tree extension with high value of the metrics, leading to the uncertainty-aware trajectory planning for a rover.

B. Uncertainty Quantification

To quantify the uncertainty collectively, first, let us define the process noise as follows:

$$\boldsymbol{w}_n \sim \mathcal{N}(\mathbf{0}, \begin{bmatrix} \sigma^2_\phi(\mathcal{M},\boldsymbol{x}_n) & 0 & 0 & 0 \\ 0 & \sigma^2_\theta(\mathcal{M},\boldsymbol{x}_n) & 0 & 0 \\ 0 & 0 & \sigma^2_s(\boldsymbol{x}_n,\boldsymbol{u}_n) & 0 \\ 0 & 0 & 0 & \sigma^2_\beta(\boldsymbol{x}_n,\boldsymbol{u}_n) \end{bmatrix}). \tag{7}$$

As in the previous work [9], the roll and pitch angles under uncertainty assumption are represented as pose bounds in the interval arithmetic [15]:

$$[\phi^-,\phi^+] = \phi^- \le \phi \le \phi^+ = [\hat{\phi} - c\sigma_{\hat{\phi}}, \hat{\phi} + c\sigma_{\hat{\phi}}], \tag{8}$$

$$[\theta^-,\theta^+] = \theta^- \le \theta \le \theta^+ = [\hat{\theta} - c\sigma_{\hat{\theta}}, \hat{\theta} + c\sigma_{\hat{\theta}}].$$

In this study, the maximum and minimum of the interval are given by the $c\sigma$ boundary, where c is defined based on the confidence level. As in [9], the pose bounds are calculated based on a probabilistic terrain model and geometrical constraint of the rover (see Supplementary Materials).

According to our prior work [14], the slip ratio and angle depend on the pose angles and vehicle steering δ in $\boldsymbol{u}_n$; therefore, the uncertainty quantification for the slip ratio and angle with the pose bounds is described as follows:

$$U_1 = \frac{1}{N_1}\int_{\phi^-}^{\phi^+}\int_{\theta^-}^{\theta^+} \sigma_s(\phi,\theta,\delta)d\phi d\theta, \tag{9}$$

$$U_2 = \frac{1}{N_2}\int_{\phi^-}^{\phi^+}\int_{\theta^-}^{\theta^+} \sigma_\beta(\phi,\theta,\delta)d\phi d\theta,$$

where N_1 and N_2 are provided by the calculation of U_1 and U_2 at the state $\boldsymbol{x}_{\text{start}}$, excluding N_1 and N_2.

C. Uncertainty Propagation

We define uncertainty propagation to consider its growth over the time steps. As in the particle-based approaches [4], uncertainty in one time step earlier affects the probability distribution of the robot state. Therefore, the uncertainty metric also needs to be strictly assessed as time passes. By combining the uncertainty quantification, two uncertainty metrics derived from U_1 and U_2 are defined as q_1 and q_2, respectively as follows:

$$q_1(\sigma_{\hat{\phi}_{n+1}}, \sigma_{\hat{\theta}_{n+1}}, \sigma_{\hat{s}_{n+1}}, 0) = (U_1 \cdot q_1(\sigma_{\hat{\phi}_n}, \sigma_{\hat{\theta}_n}, \sigma_{\hat{s}_n}, 0))^{1/\kappa}, \quad (10)$$
$$q_2(\sigma_{\hat{\phi}_{n+1}}, \sigma_{\hat{\theta}_{n+1}}, 0, \sigma_{\hat{\beta}_{n+1}}) = (U_2 \cdot q_2(\sigma_{\hat{\phi}_n}, \sigma_{\hat{\theta}_n}, 0, \sigma_{\hat{\beta}_n}))^{1/\kappa},$$
$$q_1(\sigma_{\hat{\phi}_0}, \sigma_{\hat{\theta}_0}, \sigma_{\hat{s}_0}, 0) = q_2(\sigma_{\hat{\phi}_0}, \sigma_{\hat{\theta}_0}, 0, \sigma_{\hat{\beta}_0}) = 1,$$

where κ is a coefficient for the uncertainty propagation over time; and, a smaller κ leads to higher sensitivity of the uncertainty metrics, and facilitates tuning of q_{th} for explicitly large uncertainty violation. This parameter is defined based on the magnitude of U_1 and U_2 on the motion planning scenario.

D. Slip Prediction Uncertainty

Our prior work [14] generated the vehicle model with the slip prediction based on the results of the dynamic simulation [16]. We modeled the relationship between cornering/thrust forces and vehicle slippage. In this research, the slip prediction model is rebuilt by experimental results of the robot traversing on loose terrain.

1) Traversal experiment for vehicle slippage data collection: In the rover traversing experiment, we collected a dataset of vehicle slip motions. Figure 6 demonstrates an overview of the field experiment. Several experiments were conducted with different input values for the front steering angle (δ) and traction loads (F_ϕ and F_θ) to observe a more diverse relationship between the cornering/thrust forces (F_{C} and F_{T}) and the vehicle slip ratio/angle (s and β). The traction loads and cornering/thrust forces are assumed to act as in Fig. 6 (a), and they are the same as each other for each direction when the rover is in a steady state. The experimental conditions were set as different setups of the traction loads and steering angle. δ was changed in the set of [0°, 10°, 20°, 30°]. F_ϕ was changed in the set of [-25.5 N, -11.8 N, 0 N, 11.8 N, 25.5 N]. F_θ was changed in the set of [0 N, 11.8 N, 25.5 N]. F_ϕ and F_θ are added by a constant load spring and measured using the force torque sensor mounted on the rover testbed. The command velocity v_{cmd} was constantly provided by 0.07 m/s along the x-axis of the body frame of the testbed. This experiment was conducted in the Space Exploration Field of the JAXA Sagamihara Campus [17] as illustrated in Fig. 6 (b). The test field was filled with silica sand No.5. This experimental field room was equipped with motion capture cameras, and the trace of the robot motion was measured with an accuracy of sub-millimeter order. From the trace, the longitudinal and lateral velocities of the robot (v_x and v_y) were geometrically calculated. Finally, the vehicle slip ratio and angle are obtained by the equations $s = 1 - v_x/v_{\text{cmd}}$ and $\beta = \arctan(v_y/v_x)$.

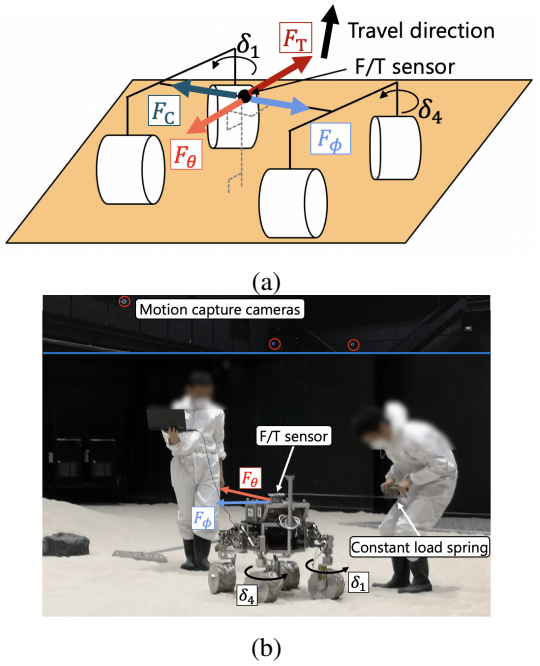

(a)

(b)

Fig. 6. Experiment to collect data on vehicle slippage. (a) Schematic view of the experimental setup. (b) Experimental setup of the robot testbed.

The collected slip ratios and angles corresponding to each experimental condition are shown in Fig. 7. In addition, cubic interpolation generated the response surfaces (s_ϕ, s_θ, β_ϕ, and β_θ) using each plot to elaborate the slip prediction model. Practically, F_ϕ and F_θ act on the rover simultaneously on rough terrain. Hence, the vehicle slippage can be approximated by combining the response surfaces in Fig. 7[1].

2) Quantification of uncertainty in slip prediction: First, standard deviations of the experimental results in Fig. 7 are calculated as σ_{s_ϕ}, σ_{s_θ}, σ_{β_ϕ}, and σ_{β_θ}. The relationship between each standard deviation and experimental conditions can be obtained as shown in Fig. 8. The traction loads is converted to pose angles by using the force-balance with gravity.

From Fig. 8, we observed that each standard deviation moderately increased as the steering angle increased. According to the plot of σ_{s_θ}, positive pitch angle increased the uncertainty. Additionally, σ_{s_ϕ} was highly increased by negative roll angles. This is presumably because the direction of negative F_ϕ is the same as the travel direction of the steered rover as shown in Fig. 6 (b), which possibly makes the robot motion unstable. Conversely, positive pose angles decreased the uncertainty for the sideslip since such conditions increased the slip ratio, as shown in Fig. 7 (a) and (b), which stabilizes the rover motion at low speeds. Thus, the heteroscedastic uncertainty in the slip prediction model is highly dependent on the vehicle posture and steering maneuvers.

Subsequently, each plot is interpolated as shown in Fig.

[1]https://codeocean.com/capsule/2372860/tree

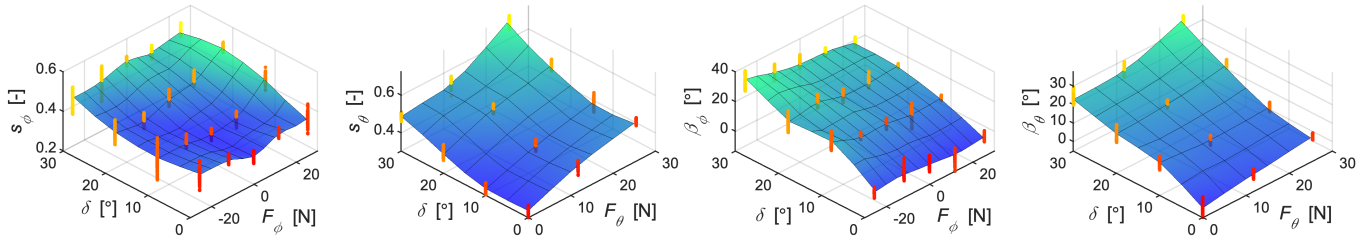

(a) F_ϕ versus s_ϕ (b) F_θ versus s_θ (c) F_ϕ versus β_ϕ (d) F_θ versus β_θ

Fig. 7. Dataset of vehicle slip motions collected in the rover traversing experiment: experimental results with a surface regression.

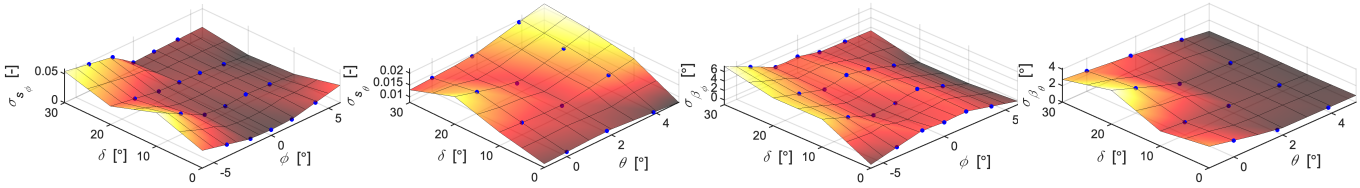

(a) ϕ versus σ_{s_ϕ} (b) θ versus σ_{s_θ} (c) ϕ versus σ_{β_ϕ} (d) θ versus σ_{β_θ}

Fig. 8. Standard deviation of the experimental results as presented in Fig. 7.

8, which depicts the standard deviation as a function of the pose and steering angles[1]. Then, σ_s and σ_β in Eq. (9) can be expressed by combining σ_{s_ϕ}, σ_{s_θ}, σ_{β_ϕ}, and σ_{β_θ}.

V. Simulation Results

A. Single Planning Step

To show the advantage of the proposed uncertainty metrics, trajectory planning simulation was conducted on two typical sets of real terrain data in Mt. Mihara[1], Japan using the following five algorithms:

- OPT for optimal trajectory without uncertainty
- CCP for chance-constraint in pose prediction [9]
- CCS for chance-constraint in slip prediction [10]
- CCPS for a combination of CCP and CCS
- UM for the proposed uncertainty metrics

(CCP), (CCS), and (CCPS) extended the tree under the chance-constraint fashion in the traversability prediction with a probability of 86.6 %. Conversely, (UM) set q_{th} as 5.0 for uncertainty-awareness. Table II summarizes other parameters used for the trajectory-planning simulations. The threshold of the rover pose angle and slippage can be derived from the mobility performance of the testbed. The proposed trajectory planning algorithm was implemented in Python and ran on a computer with an Intel i5 CPU 2.0 GHz processor. These hyperparameters were adjusted to be the most conservative values among those for which trajectories can be found in our scenarios. As the CL-RRT$^\#$ algorithm is a randomized sampling-based algorithm, trajectory planning was conducted for five trials on real terrain maps. Each result is presented in Figs. 9 (a) and (b), where cost-minimum trajectories are shown due to simplicity. Figures 9 (c) and (d) show the total cost and maximum uncertainty metrics for each algorithm. Figures 9 (e) and (f) present the computational cost normalized by the computation time of (OPT).

TABLE II

Parameters used in trajectory planning simulation.

Parameter	Value	Unit
ϕ_{th}, N_ϕ	20.0	degrees
$\theta_{\text{th}}, N_\theta$	20.0	degrees
s_{th}, N_s	0.90	-
$\beta_{\text{th}}, N_\beta$	45.0	degrees
N_L	1.0	m
W_L	0.20	-
W_ϕ, W_θ	0.30	-
W_s	0.05	-
W_β	0.15	-
κ	2.0	-
c	1.5	-

(OPT) and (CCS) found trajectories with lower cost among the five algorithms, which directly approached the given goal. (CCP), (CCPS), and (UM) only found trajectories that detoured the area traversed by (OPT) and (CCS). This result implies that the proposed metrics and chance-constraint generate uncertainty-aware trajectories. Notably, (UM) did not find the minimum cost trajectory, whereas its uncertainty metrics were small compared with other algorithms. For computational cost, the runtime of (UM) was almost the same as that of (OPT). We deduce that this is because (UM) computes the uncertainty metrics only by numerical integration in the CL-RRT$^\#$ procedure. This implies that the proposed algorithm can run in real time, since the runtime of the conventional CL-RRT and CL-RRT$^\#$ has been verified in real time [13]. Notably, the particle-based approach and the state-of-the-art [12] are not tested because they require a lot of computational time or GPUs. They should require a computation cost of $1.0 \times n$.

For further evaluation, the Monte Carlo method was used. Monte Carlo simulations for each algorithm were performed 500 trials. In each simulation, the rover traversed along the nominal trajectory; however, each state was statistically

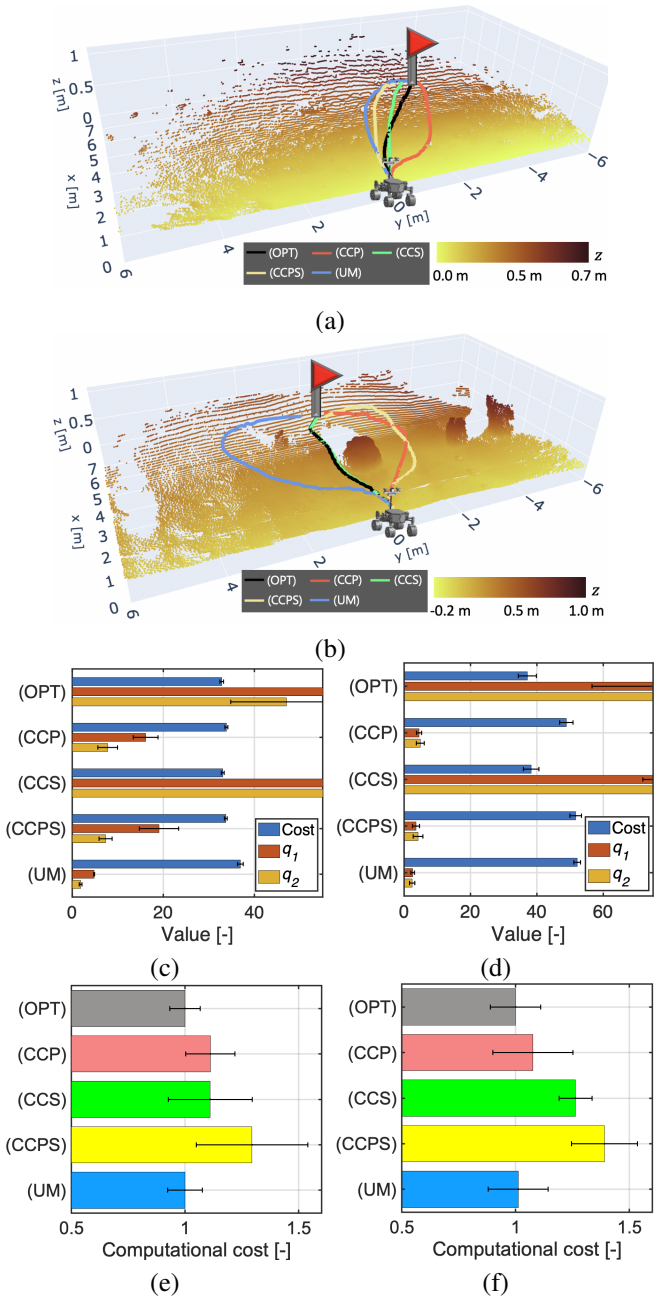

Fig. 9. Results of trajectory planning simulation on real terrain. (a) Trajectories in Scenario (1). (b) Trajectories in Scenario (2). Red flags represent the goal area. (c) and (d) Total cost and maximum uncertainty metrics in Scenarios (1) and (2). (e) and (f) Computational costs normalized by the averaged time of (OPT) such that about 1.0 means that algorithm run in real time.

calculated based on a random sampling from the slip prediction model and wheel-terrain contact model [9]. Table III summarizes the mean and standard deviation values of the worst value of the traversability indices for 500 trials on each algorithm. The navigation success rate is defined as the rate of the number of trajectories that can successfully reach the goal without mobility hazards, defined by the case where each traversability index is larger than the threshold ϕ_{th}, θ_{th}, s_{th}, and β_{th}.

As compared with (OPT), (CCP), and (CCS), (CCPS)

TABLE III

RESULTS OF THE TRAJECTORY EVALUATION. THE WORST VALUE IN A SINGLE TRIAL IS SUMMARIZED FOR EACH TRAVERSABILITY INDEX.

(a) Scenario (1)

	Success [%]	Roll angle [◦]	Pitch angle [◦]	Slip ratio [-]	Slip angle [◦]
(OPT)	39.8	16.81 ± 4.63	15.82 ± 3.21	0.836 ± 0.087	28.21 ± 12.79
(CCP)	54.4	14.98 ± 5.47	14.30 ± 3.73	0.826 ± 0.089	28.78 ± 10.97
(CCS)	36.2	16.47 ± 4.79	17.23 ± 3.09	0.833 ± 0.079	27.38 ± 11.99
(CCPS)	78.7	12.21 ± 4.46	13.04 ± 3.33	0.790 ± 0.077	24.32 ± 9.04
(UM)	98.2	9.74 ± 1.85	9.71 ± 1.81	0.745 ± 0.049	22.60 ± 5.04

(b) Scenario (2)

	Success [%]	Roll angle [◦]	Pitch angle [◦]	Slip ratio [-]	Slip angle [◦]
(OPT)	8.4	17.75 ± 5.16	16.98 ± 4.14	0.849 ± 0.082	31.84 ± 13.97
(CCP)	67.6	14.23 ± 2.98	12.58 ± 2.08	0.808 ± 0.073	35.03 ± 12.06
(CCS)	13.8	18.83 ± 4.89	15.77 ± 3.59	0.841 ± 0.083	32.79 ± 14.26
(CCPS)	68.2	12.90 ± 5.11	10.80 ± 3.55	0.768 ± 0.084	30.70 ± 10.21
(UM)	84.0	10.54 ± 3.52	10.17 ± 2.81	0.757 ± 0.084	27.32 ± 9.67

improved the success rate and all values of the traversability indices as it considered both uncertainties in the pose and slip predictions. However, the success rate was less than 86.6 %, implying that the chance-constraint approach for nominal states does not guarantee the confidence level of the safety against the mobility hazards in heteroscedastic uncertainty assumption as discussed in the problem formulation. In a real rover mission, this fact could be a critical problem. Conversely, (UM) outperformed other algorithms in success rate and traversability indices. Notably, the proposed uncertainty metrics mitigated the growth of uncertainty, resulting in the reduction of the probability of mobility hazards.

B. Multiple Planning Steps

To show the applicability of the uncertainty metrics, we propose (CCPS w/ UM) as the hybrid method of (CCPS) and (UM), wherein the proposed uncertainty metrics is used as additional constraint to the chance-constraint approach. To examine the effect of the uncertainty metrics when incorporated into the chance-constraint approach, (CCPS w/ UM) is compared with (CCPS) in a long-range navigation scenario, which includes diverse geological features. The terrain map is given by a fractal approach [18], which is widely used for the validation of motion planners [10], [19]. Figure 10 (a) shows the result of the trajectory planning simulation. Each planner sequentially generated a trajectory towards each waypoint in the figure. Furthermore, 1000 trials of the Monte Carlo simulations were performed again. Figures 10 (b) and (c) summarize the result of the success rate and uncertainty metrics. Let us denote the start, waypoints, and goal in order as waypoint #[0, 1, 2, 3, 4, 5, 6].

From waypoint #0 to waypoint #4, (CCPS w/ UM) outperformed (CCPS) in success rate. We deduce that this is because the trajectories of (CCPS w/ UM) maintains lower values for the uncertainty metrics. This implies that the uncertainty metrics can enhance the chance-constraint approach to avoid the risk of unexpected mobility hazards.

Conversely, (CCPS w/ UM) slightly deteriorated in success rate from waypoint #4 to waypoint #6 although its uncertainty metrics were smaller than that of (CCPS). This could be explained by Fig. 4. As shown in Fig. 10 (a), the terrain feature around waypoints #4 $\sim$ #6 is relatively moderate. Thus, (CCPS) did not encounter mobility hazards even for distributions with large uncertainty, such as the

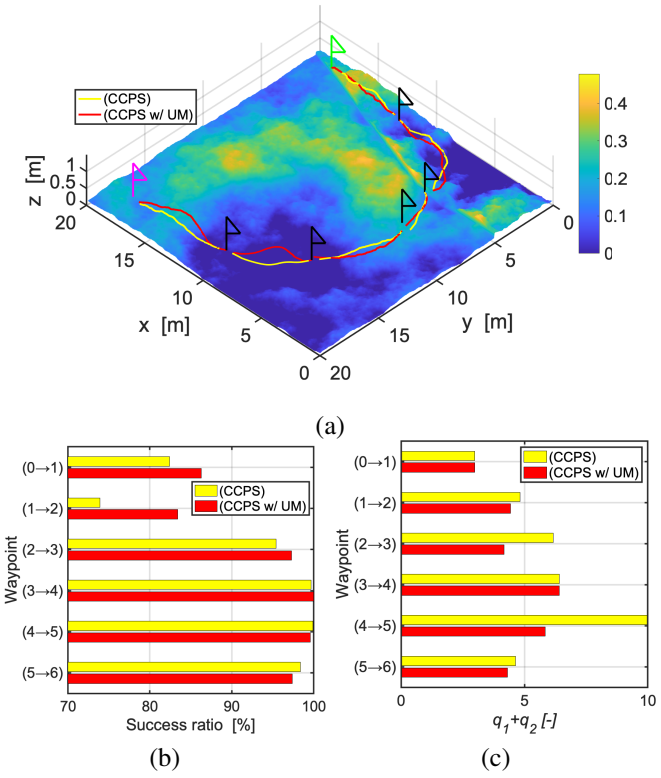

Fig. 10. Results of trajectory planning and evaluation of (CCPS) and (CCPS w/ UM) in long range navigation. (a) Trajectories on fractal terrain. Each waypoint is given by the black flag. The start and goal area are colored by green and magenta, respectively. Color bar represents terrain height. (b) Success rate between waypoints. (c) Total uncertainty metrics between waypoints.

probability distribution depicted by the green dashed line. Conversely, (CCPS w/ UM) can avoid large uncertainty colored by magenta and green; however, it preferred the probability distribution with relatively large nominal value of traversability index $\hat{\lambda}$ as shown in blue. As a result, the success rate of (CCPS w/ UM) seemed to be worse. Indeed, the proposed uncertainty metrics can exclude the distribution depicted by the green solid line, which has relatively large traversability index with large uncertainty; however, the metrics may not perform well in flat but uncertain terrain.

This can be improved by dynamically changing q_{th} based on the nominal state $\hat{\boldsymbol{x}}$. For instance, q_{th} should be set to 10.0 on flat terrain such as waypoints #4 $\sim$ #6, whereas a smaller value of q_{th} is preferable in challenging environments.

VI. Conclusion and Future Work

In this study, we proposed the uncertainty-aware trajectory planning algorithm for a planetary exploration rover to reduce the probability of vehicle rollover and extremely high slip on rough and loose terrains. The proposed algorithm incorporated the basic CL-RRT$^{\#}$ algorithm with the uncertainty metrics, which consist of uncertainty quantification and propagation in rover traversability prediction. Notably, the vehicle slippage was experimentally measured in high-slip terrain to quantify heteroscedastic uncertainty. Simulation results on real terrains revealed that the proposed metrics can work in the same runtime of the basic CL-RRT$^{\#}$, and can outperform the chance-constraint approach in traversability prediction by up to 20 %. Further, simulations of long-range traversing on fractal terrain showed that the combination of the proposed metrics and chance-constraint formulation can improve navigation success on more challenging terrain.

A possible direction for future work includes the modeling of the best q_{th} for each situation. This could enable the performance of the proposed metrics to be adjusted even for flat but uncertain terrain, which is a weakness of the proposed planner.

Future studies will also include the applicability of the uncertainty metrics on unknown environments with different soil types. Uncertainty in unknown environments can be quantified using the model generated in a known environment, but the accuracy will be lower. This could be improved by transfer learning methods as in [20], wherein pre-generated traversability/uncertainty models can be adapted to new environments.

Acknowledgments

The authors would like to thank Naohiro Enokida for his help with experiments on vehicle slippage data collection in the Space Exploration Field of the JAXA Sagamihara Campus. We also thank the Space Exploration Innovation Hub Center for providing the opportunity to collect the slip data.

References

[1] P. Papadakis, "Terrain traversability analysis methods for unmanned ground vehicles: A survey," *Engineering Applications of Artificial Intelligence*, vol. 26, no. 4, pp. 1373–1385, 2013.

[2] J. J. Biesiadecki and M. W. Maimone, "The Mars Exploration Rover Surface Mobility Flight Software: Driving Ambition," in Proc. of *2006 IEEE Aerospace Conference*, pp. 4–11, 2006.

[3] N. A. Melchior and R. Simmons, "Particle RRT for path planning with uncertainty," in Proc. of *IEEE International Conference on Robotics and Automation*, pp. 1617–1624, 2007.

[4] M. Mizuno and T. Kubota, "A New Path Planning Architecture to Consider Motion Uncertainty in Natural Environment," in Proc. of *IEEE International Conference on Robotics and Automation*, pp. 2182–2188, 2020.

[5] G. Kewlani, G. Ishigami, and K. Iagnemma, "Stochastic mobility-based path planning in uncertain environments," in Proc. of *IEEE/RSJ International Conference on Intelligent Robots and Systems*, pp. 1183–1189, 2009.

[6] A. Bry and N. Roy, "Rapidly-exploring random belief trees for motion planning under uncertainty," in Proc. of *IEEE International Conference on Robotics and Automation*, pp. 723–730, 2011.

[7] J. Berg, P. Abbeel, and K. Goldberg, "LQG-MP: Optimized Path Planning for Robots with Motion Uncertainty and Imperfect State Information," *The International Journal of Robotics Research*, vol. 30, no. 7, pp. 895–913, 2011.

[8] S. U. Lee, R. Gonzalez, and K. Iagnemma, "Robust sampling-based motion planning for autonomous tracked vehicles in deformable high slip terrain," in Proc. of *IEEE International Conference on Robotics and Automation*, pp. 2569–2574, 2016.

[9] K. Otsu, G. Matheron, S. Ghosh, O. Toupet, and M. Ono, "Fast Approximate Clearance Evaluation for Rovers with Articulated Suspension Systems," *Journal of Field Robotics*, vol. 37, no. 5, pp. 768–785, 2020.

[10] H. Inotsume, T. Kubota, and D. Wettergreen, "Robust Path Planning for Slope Traversing under Uncertainty in Slip Prediction," *IEEE Robotics and Automation Letters*, vol. 5, no. 2, pp. 3390–3397, 2020.

[11] A. Candela and D. Wettergreen, "An Approach to Science and Risk-Aware Planetary Rover Exploration," *IEEE Robotics and Automation Letters*, vol. 7, no. 4, pp. 9691–9698, 2022.

[12] X. Cai, M. Everett, L. Sharma, P. R. Osteen, and J. P. How, "Probabilistic Traversability Model for Risk-Aware Motion Planning in Off-Road Environments," *arXiv:2210.00153*, 2022.

[13] O. Arslan and P. Tsiotras, "Sampling-based Algorithms for Optimal Motion Planning Using Closed-loop Prediction," in Proc. of *IEEE International Conference on Robotics and Automation*, pp. 4991–4996, 2017.

[14] R. Takemura and G. Ishigami, "Traversability-based Trajectory Planning with Quasi-Dynamic Vehicle Model in Loose Soil," in Proc. of *IEEE/RSJ International Conference on Intelligent Robots and Systems*, pp. 8388–8394, 2021.

[15] T. Hickey and M. H. V. Emden, "Interval Arithmetic : from Principles to Implementation," *Journal of the ACM*, vol. 48, no. 5, pp. 1038–1068, 2001.

[16] G. Ishigami and K. Yoshida, "Steering Characteristics of an Exploration Rover on Loose Soil based on All-Wheel Dynamics Model," in Proc. of *IEEE/RSJ International Conference on Intelligent Robots and Systems*, pp. 2041–2046, 2005.

[17] JAXA, "Space Exploration Innovation Hub Center." http://www.ihub-tansa.jaxa.jp/english/index.html

[18] Y. Yokokohji, S. Chaen, and T. Yoshikawa, "Evaluation of traversability of wheeled mobile robots on uneven terrains by fractal terrain model," in Proc. of *IEEE International Conference on Robotics and Automation*, vol. 3, pp. 2183–2188 Vol.3, 2004.

[19] W. Fink, V. R. Baker, M. Flammia, and M. A. Tarbell, "Rover traverse-optimizing planner for multi-objective deployment scenarios," *IEEE Aerospace Conference Proceedings*, vol. 2015-June, no. 1, pp. 1–9, 2015.

[20] H. Inotsume and T. Kubota, "Adaptive Terrain Traversability Prediction based on Multi-Source Transfer Gaussian Processes," in Proc. of *IEEE/RSJ International Conference on Intelligent Robots and Systems*, pp. 2274–2281, 2021.